Hydrodynamics of fingering instabilities in dipolar fluids

David P. Jackson and Raymond E. Goldstein
Department of Physics, Joseph Henry Laboratories, Princeton University, Princeton, New Jersey 08544

Andrejs O. Cebers
Latvian Academy of Science, Riga, Latvia
(Received 2 February 1994)

Domains of magnetic and electric dipolar fluids are known to undergo fingering instabilities in Hele-Shaw flow, forming complex labyrinthine patterns. The hydrodynamics of this process are studied theoretically with a generalization of Darcy's law. The boundary condition on the pressure at the interface between the dipolar fluid and that surrounding it is shown to include competing Young-Laplace and Biot-Savart terms. The spectrum of growth rates in the linear stability analysis of a circular domain has a complicated wave vector dependence as a consequence of the long-range forces, and reveals that the fingering arises from a negative effective surface tension. The free boundary problem for the interface motion is solved numerically using conformal mapping methods, and is compared with experiment. A simple model is proposed for mode competition and pattern selection under time-dependent magnetic fields. Aspects of this analysis may be relevant to the description of the intermediate state of type-I superconductors.

PACS number(s): 47.20.−k, 68.10.−m, 75.70.Kw

I. INTRODUCTION

The long-time behavior of driven dissipative systems characterized by an interfacial instability is typically either *steady* (in an absolute or statistical sense) or *stationary*. Examples of the former are viscous fingering phenomena in Hele-Shaw flow and diffusion-limited aggregation. In such systems, the fundamental question of pattern selection centers on the chosen wavelength of cellular structures [1], finger width in a channel geometry [2], or the fractal dimension of a growing cluster [3]. We may term such systems *open* in the sense that the volume enclosed by the evolving interface varies with time, reflecting either a fixed pressure difference or fixed flux. Less well explored are systems whose interfaces are *closed* with respect to volume changes, typified by those in which the bounded fluid is incompressible. In these systems, nontrivial patterns often arise from a competition between surface tension and body forces (e.g., centrifugal [4] or gravitational [5]).

We discuss here interfacial instabilities in Hele-Shaw flow driven by the competition between surface tension and long-range dipolar forces, and which, following a complex dynamical process, appear to result in a variety of stable *stationary* states. The dipolar interactions arise from the magnetization of an incompressible ferrofluid [6] by an external magnetic field. They could equally well arise from the polarization of a dielectric fluid in an external electric field [7], or from the oriented permanent dipoles of amphiphilic molecules in Langmuir monolayers [8,9]. The equilibrium states have been observed by several groups [6,10–13] and are qualitatively different from the steady states mentioned above. A recent systematic study of fingering instabilities in magnetic fluids [12] has revealed a surprisingly large array of possible branched treelike shapes, some of which are shown in the left-hand panel of Fig. 1. An earlier treatment of this problem [14] studied the connection between these competing forces and the motion of the domain boundary in the simplest gradient-flow model. There, the hydrodynamics of the medium enters only to the extent that it provides viscous dissipation, which was further assumed to be localized at the interface. In reality, the viscous dissipation takes place throughout the domain, as described approximately by Darcy's law [15], and the interfacial

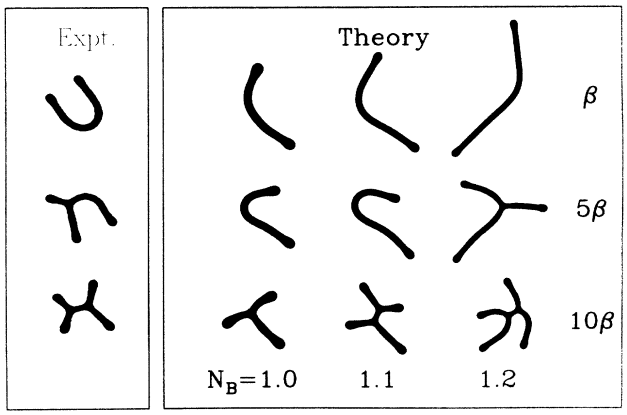

FIG. 1. Experimental and theoretical final state patterns. The left panel is from the experimental work of Dickstein, Erramilli, and Goldstein [32], showing the variety of patterns obtained following rapid steps in the magnetic field. The theoretical shapes, obtained from numerical solution of Eq. (19) with $p=20$, are arranged according to the values of N_B and the ramp rate β. As in experiment, higher magnetic fields lead to thinner fingers, and higher ramp rates lead to more branching.

motion is determined *nonlocally* because of the fluid's incompressibility.

In Sec. II we describe a generalization of Darcy's law to the flow of dipolar fluids and show that the resulting interface dynamics is a gradient flow. Section III is a discussion of the solution to the free-boundary problem by means of conformal mapping techniques [16], the linear stability analysis for circular shapes, and aspects of pattern selection which have appeared in an earlier short communication [12]. The qualitative similarity of the theoretical patterns seen in the rest of Fig. 1 and in Fig. 2, obtained from the theory outlined herein, suggest the validity of the simple model proposed for this competition of forces.

A fundamental feature of this system is that not only is the interface motion determined nonlocally, but the ferrofluid is subjected to a body force which is also intrinsically nonlocal. In the simplest model, valid for any uniformly dipolar fluid, this force may be recast as a self-interaction of the boundary having the form of the Biot-Savart force of a current carrying ribbon. The nonlocal nature of the applied force allows for a secondary structure of "fingers" to develop, each having a characteristic field-dependent width (Fig. 1). These are in turn connected via threefold nodes into a tertiary treelike structure. Such branched domain patterns are found as well in many magnetic systems [17] and in the intermediate state of type-I superconductors in thin-film geometry [18]. In light of the usual correspondence between magnetization and current loops, this similarity is to be anticipated, the superconducting Meissner currents being localized at the superconductor-normal metal interfaces which are the boundaries of the domains. It is these currents that provide the perfect diamagnetism characteristic of superconductors. We return to these systems in the concluding section IV.

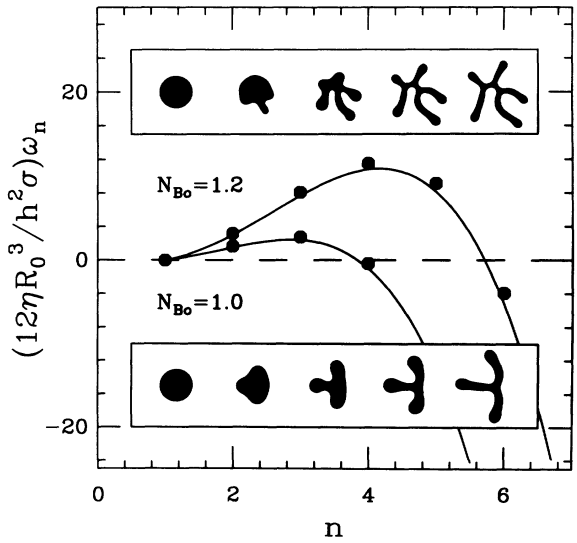

FIG. 2. Linear growth rate as a function of mode number for $N_B=1.0$ and 1.2 with $p=20$. The solid circles show the exact result from Eqs. (22) and (23), while the curves are the Bessel function approximations. The upper and lower insets show shape evolutions following instantaneous steps to the two values of N_B.

II. DARCY'S LAW FOR DIPOLAR FLUIDS

A. Formulation

We proceed first to define the experimental geometry. The ferrofluid domain is trapped between two horizontal glass plates separated by a distance h and surrounded by another fluid with which it is immiscible, such as water. In the absence of an applied field, the equilibrium shape of the ferrofluid is determined solely by surface tension to be that with minimum surface area for a given volume; when viewed from above, this shape is clearly a circle. A magnetic field $\mathbf{H}_0=H_0\hat{\mathbf{e}}_z$ is then applied perpendicular to the plates and the resulting motion is seen as a two-dimensional area-preserving evolution.

To study the problem, we assume the dipole alignment is along the direction of the applied field, and is a function only of its magnitude. The net result is a uniformly distributed array of dipoles, the strength of which is determined from the applied field $\mathbf{M}(\mathbf{H})=M(H_0)\hat{\mathbf{e}}_z$. This approximation has been used by others [10,14,19,20] and amounts to the study of the fringing fields of a parallel plate capacitor. Here we use the lowest nonvanishing contribution to write

$$H\simeq H_0-\frac{\partial\psi}{\partial z}\ , \tag{1}$$

where $\psi(x,y,z)$ is the magnetic scalar potential found by introducing a fictitious "magnetic charge density" $\sigma_M=\mathbf{M}\cdot\hat{\mathbf{n}}$, where $\hat{\mathbf{n}}$ is normal to the planar surfaces of the domain [21].

Under these approximations, and with the neglect of inertial terms, the Navier-Stokes equation for the magnetic fluid [6] becomes

$$\mathbf{0}=-(\nabla P-M\nabla H)+\eta\nabla^2\mathbf{v}\ . \tag{2}$$

Here, P is the pressure of the fluid and η is its viscosity. The magnetic term $M\nabla H$ is reminiscent of the Kelvin force density [6,21] except H here represent the local field as opposed to the applied field. Following the standard approach in Hele-Shaw problems, we take a parabolic velocity profile vanishing on the plate boundaries, and then average over the perpendicular direction to obtain [16,22]

$$\mathbf{v}=-\frac{h^2}{12\eta}\nabla\Pi\ , \tag{3}$$

where

$$\Pi=\frac{1}{h}\int_0^h P(x,y,z)dz+\frac{2M}{h}\psi(x,y,h) \tag{4}$$

and $\mathbf{v}(x,y)$ is a z-averaged quantity.

Equation (3) represents the Darcy approximation for a magnetic fluid, and, when $M=0$, is identical to the equation obtained for a nonmagnetic fluid. Within the assumptions of Darcy's law, the precise form of the equation of motion for the ferrofluid-water boundary depends on the relative viscosities η_1 and η_2 of the ferrofluid and water, respectively, as described in Appendix A. Here we

consider perhaps the conceptually simplest case, where the outer fluid is taken to have a negligible viscosity. Then the external pressure may to a good approximation be assumed constant (say, zero). We are then left to solve a Dirichlet problem for a simply connected region, the interior of the domain $\mathcal{D}$, in which $\nabla^2\Pi=0$ by the incompressibility constraint. If α is an arbitrary parametrization of the interface $\mathcal{C}$, then the boundary condition is

$$\Pi(\alpha)|_{\mathcal{C}}=\sigma\kappa(\alpha)+\frac{2M^2}{h}I(\alpha)\ , \tag{5}$$

where σ is the surface tension and κ is the curvature of the interface. The magnetic integral $I(\alpha)$ may be expressed in three equivalent forms. The first derives from the interpretation of the magnetic scalar potential in Eq. (1) as that arising from magnetic charge along the top and bottom surfaces of the domain:

$$I(s)=\int_{\mathcal{D}}dA'\left[\frac{1}{\sqrt{(x-x')^2+(y-y')^2}}-\frac{1}{\sqrt{(x-x')^2+(y-y')^2+h^2}}\right]\ . \tag{6}$$

where $x=x(\alpha)$ and $y=y(\alpha)$ are the components of $\mathbf{r}(\alpha)$. A second form for I derives from the relation between magnetization and current loops [14], $\mathbf{J}=c\mathbf{M}\times\hat{\mathbf{n}}$,

$$I(s)=\oint_{\mathcal{C}}ds'\hat{\mathbf{R}}\times\hat{\mathbf{t}}(s')[\sqrt{1+(h/R)^2}-1]\ . \tag{7}$$

Here, $\hat{\mathbf{t}}$ is the unit tangent vector to the curve at arclength s, and $\mathbf{R}$ is the vector $\mathbf{r}(s)-\mathbf{r}(s')$. A third form, useful in computation, is

$$I(\alpha)=\oint_{\mathcal{C}}dx'\ln\left\{\frac{(y-y')+R}{(y-y')+\sqrt{R^2+h^2}}\right\}\ , \tag{8}$$

where $x=x(\alpha)$, $x'=x(\alpha')$, etc., and

$$R^2=(x-x')^2+(y-y')^2\ .$$

The equivalence between these forms is shown in Appendix B.

The first term in Eq. (5) is simply the excess ("Young-Laplace") pressure of an interface with surface tension, while the second is the magnetic contribution. As noticed previously [14], this term is simply the Biot-Savart force of a current carrying ribbon on itself. Taken together, these imply a generalization of the interfacial condition (see also [23]) given by

$$h\,\Pi(\alpha)|_{\mathcal{C}}=\frac{1}{\sqrt{g}}\hat{\mathbf{n}}\cdot\frac{\delta\mathcal{E}}{\delta\mathbf{r}}\ , \tag{9}$$

where $g=\mathbf{r}_\alpha\cdot\mathbf{r}_\alpha$ is the metric and $\mathcal{E}$ is the energy functional of an arbitrary shaped dipolar domain of height h and contour length L [14,24]:

$$\mathcal{E}=\sigma hL-M^2h\oint_{\mathcal{C}}ds\oint_{\mathcal{C}}ds'\hat{\mathbf{t}}(s)\cdot\hat{\mathbf{t}}(s')\Phi(R/h)\ , \tag{10}$$

with

$$\Phi(\xi)=\sinh^{-1}(1/\xi)+\xi-\sqrt{1+\xi^2}$$

and

$$R=|\mathbf{R}|=|\mathbf{r}(s)-\mathbf{r}(s')|\ .$$

In Appendix B we recall [14] that the origin of the function Φ is integration over the thickness of the slab of the standard form for self-inductance, and that the familiar form for a wire loop is recovered for $R/h\gg1$.

B. Darcy's law as a gradient flow

The generalization of the interfacial boundary condition in Eq. (9) still preserves an essential aspect of viscously overdamped motion described by Darcy's law, namely, that it is a *gradient flow* [25]. That is, when the energy may be expressed as a functional $\mathcal{E}[\mathbf{r}]$ of the position of the boundary in two-phase Darcy's law flow, then $\mathcal{E}$ is a decreasing function of time. This is true independent of whether $\mathcal{E}$ is a local or nonlocal functional of the boundary. To establish this, first decompose the velocity of the moving contour into the local Frenet-Serret frame, of unit normal $\hat{\mathbf{n}}$ and tangent $\hat{\mathbf{t}}$,

$$\mathbf{r}_t=U\hat{\mathbf{n}}+W\hat{\mathbf{t}}\ . \tag{11}$$

For an arbitrary functional $\mathcal{F}[\mathbf{r}]$ whose functional derivative $\delta\mathcal{F}/\delta\mathbf{r}$ is in the normal direction, we obtain the general relation

$$\mathcal{F}_t=\oint_{\mathcal{C}}ds\frac{1}{\sqrt{g}}\hat{\mathbf{n}}\cdot\frac{\delta\mathcal{F}}{\delta\mathbf{r}}U\ , \tag{12}$$

where $ds=d\alpha\sqrt{g}$. Two well-known special cases of this result pertain to the evolution of the area A and length L of a closed curve in the plane. With $\delta A/\delta\mathbf{r}=\sqrt{g}\,\hat{\mathbf{n}}$ and $\delta L/\delta\mathbf{r}=\sqrt{g}\,\kappa\hat{\mathbf{n}}$, we obtain

$$A_t=\oint_{\mathcal{C}}ds\,U,\quad L_t=\oint_{\mathcal{C}}ds\,\kappa U\ . \tag{13}$$

Consider first the case in which the outer fluid is, say, air, having negligible viscosity ($\eta_2=0$) and vanishing external pressure. Then we identify Π in Eq. (9) as the limiting value of the pressure as the interface is approached from the interior of the fluid domain. Using Darcy's law for the fluid velocity on the boundary (equal to the interface velocity), we may write

$$\mathcal{E}_t=-\frac{h^2}{12\eta_1}\oint_{\mathcal{C}}ds\,\Pi(s)\hat{\mathbf{n}}\cdot\nabla\Pi\ . \tag{14}$$

An integration by parts allows this to be expressed as an area integral over the domain

$$\begin{aligned}\mathcal{E}_t&=-\frac{h^2}{12\eta_1}\int_{\mathcal{D}}dA(\nabla\Pi)^2\\&=-\frac{12\eta_1}{h^2}\int_{\mathcal{D}}dA\,\mathbf{v}^2\\&\le0\ .\end{aligned} \tag{15}$$

The energy thus decreases monotonically in time, reaching a stationary value only when the pressure is constant, at which point the fluid velocity vanishes. Note [26] that the dissipation is proportional to the square of the local (z-averaged) fluid velocity in Darcy's law (3), rather than

being related to velocity *gradients* as in the full Navier-Stokes equations. This lack of Galilean invariance in the dissipation associated with Darcy's law arises, of course, from the no-slip boundary conditions on the upper and lower plates.

In the more general case of nonzero external viscosity, the analysis proceeds as above, except that we identify the functional derivative of the energy with the *jump* in the pressure across the interface:

$$h\,[\Pi_1(\alpha)|_{\mathcal{C}}-\Pi_2(\alpha)|_{\mathcal{C}}]=\frac{1}{\sqrt{g}}\hat{\mathbf{n}}\cdot\frac{\delta\mathcal{E}}{\delta\mathbf{r}}\ , \tag{16}$$

Then the energy evolves as

$$\mathcal{E}_t=\oint_{\mathcal{C}} ds(\Pi_1-\Pi_2)U\ , \tag{17}$$

which by the divergence theorem and the kinematic boundary condition $\hat{\mathbf{n}}\cdot\mathbf{v}_1=\hat{\mathbf{n}}\cdot\mathbf{v}_2$ in the interface leads to

$$\begin{aligned}\mathcal{E}_t=&-\frac{h^2}{12\eta_1}\int_{\mathcal{D}} dA(\nabla\Pi)^2\\&-\frac{h^2}{12\eta_2}\int_{O} dA(\nabla\Pi)^2\\&\le 0\ ,\end{aligned} \tag{18}$$

where O is the domain outside the contour $\mathcal{C}$.

III. INTERFACE DYNAMICS

A. Conformal mapping

The evolution of the interface is given by the condition that its normal velocity be that of the fluid, while the tangential velocity is as yet unspecified. Since tangential motions have no physical meaning, we may choose a tangential velocity for computational convenience. The solution to the Dirichlet problem is known on the unit disk, and we use conformal mapping techniques to map that solution to the domain of interest. The interface evolution equation then becomes one for the map itself [16]. If the interface is described in the complex plane by the function $\rho(\alpha)$, then

$$\partial_t\rho=i(\partial_\alpha\rho)\mathcal{A}\left\{\frac{\mathrm{Re}[z\partial_z\mathcal{A}\{\Pi\}]_{e^{i\alpha}}}{|\partial_\alpha\rho|^2}\right\}\Bigg|_{z=e^{i\alpha}}\ . \tag{19}$$

The integral operator $\mathcal{A}$ is similar to the Poisson integral but takes a real function $\Pi(\alpha)$ and returns an analytic function whose real part evaluated at $e^{i\alpha}$ is $\Pi(\alpha)$. This is most easily seen as follows: Given

$$\Pi(\alpha)=a_0+\sum(a_n e^{in\alpha}+a_n^* e^{-in\alpha})\ , \tag{20}$$

then

$$\mathcal{A}\{\Pi(\alpha)\}=a_0+2\sum a_n z^n\ . \tag{21}$$

The dynamical variables in the problem are thus the Fourier coefficients a_n.

B. Linear stability analysis

To determine the stability of the initial shape, we linearize Eq. (19) in the amplitude of small disturbances about a circle. Setting

$$\gamma(\theta,t)=[R_0+\sum_n \zeta_n\cos n\theta\exp(\omega_n t)]e^{i\theta}$$

and solving to lowest order in ζ_n/R_0, we obtain

$$\omega_n=\frac{h^2\sigma}{12\eta R_0^3}|n|[(1-n^2)+p^2N_B\mathcal{D}_n(p)]\ , \tag{22}$$

where

$$\mathcal{D}_n(p)=\sum_{k=2}^{n}\frac{1}{2k-1}+\frac{p}{2}\int_0^{\pi/2}\frac{\cos(2n\omega)-\cos(2\omega)}{\sqrt{1+p^2\sin^2\omega}}d\omega\ , \tag{23}$$

and we have found it convenient to use the dimensionless numbers

$$p=2R_0/h\quad\text{and}\quad N_B=2M^2h/\sigma\ . \tag{24}$$

The first is simply a geometric aspect ratio, while the second is a magnetic Bond number, giving the relative strength of dipolar to surface forces.

The form of Eq. (22) is identical to that obtained in an earlier work [14], except for the overall factor of $|n|/R_0$ and the particular coefficients in the prefactor $h^2\sigma/12\eta R_0^3$. This modified n dependence arises from the fact that in Darcy's law the velocity is proportional to *gradients* of pressure, whereas in the local dissipation model, it is proportional to the pressure itself [27]. Figure 2 shows the function ω_n for $p=20$ and two values of N_B. Note that $\omega_1=0$, since this mode corresponds to a translation of the circle, and that the peak location and width of the band of unstable modes increase with increasing Bond number. At fields high enough that there is more than one unstable mode, the competition between those modes can translate slight variations in initial conditions into large differences in the final shapes. Shown as insets in Fig. 2 are shape evolutions at the two values of N_B, obtained from the conformal mapping approach. There is a strong correlation between the number of arms in the final shape and the fastest growing mode from the dispersion relation. Such instantaneous jumps cannot be realized experimentally. Rather, the field is ramped to its final value. Section III C discusses the consequences of this ramping in more detail.

We may gain some physical insight into the mechanism of the instability by considering the case of *thin* layers ($p\gg 1$) and using the aysmptotic properties of the integrals in Eq. (23) established by Thiele [28]. We obtain

$$\begin{aligned}\omega_n\simeq\frac{h^2\sigma|n|}{12\eta R_0^3}\Bigg\{&(n^2-1)-\tfrac{1}{2}N_B\Bigg[(n^2-1)[\ln(4p)-1]\\&+(\tfrac{1}{2}-2n^2)\sum_{j=2}^{n}\frac{1}{2j-1}\Bigg]\Bigg\}\\&+O(1/p^2)\ .\end{aligned} \tag{25}$$

The complicated dependence on the mode number in Eq. (25) reflects the long-range dipolar forces. An accurate analytic approximation in this limit is [14]

$$\mathcal{D}_n(p)\simeq\tfrac{1}{2}[\ln(n)+K_0(2n/p)-K_0(2/p)]\ ,$$

which may be manipulated to yield

$$\omega_n\simeq\frac{h^2\sigma|n|}{12\eta R_0^3}((1-n^2)\{1-\tfrac{1}{2}N_B[1+\ln(p)-C]\}$$
$$-\tfrac{1}{2}N_B n^2\ln(n))\ , \qquad (26)$$

where $C\approx 0.577\,21\ldots$ is Euler's constant. Apart from the final term, there is a common factor of $|n|(1-n^2)$, which, upon review of Eq. (22), comes from the curvature, thus indicating the interpretation of an effective tension

$$\sigma_{\text{eff}}=\sigma\{1-\tfrac{1}{2}N_B[1-C+\ln(p)]\}\ , \qquad (27)$$

a result established in [14] in the context of the local model of dissipation and by De Koker and McConnell by similar means [29]. From this, we deduce the critical Bond number for a negative tension:

$$N_B^*\simeq 2/[1-C+\ln(p)]\ .$$

Of particular interest is the most unstable mode n^* as a function of magnetic Bond number, which from the approximation (26) is expected to have an exponential dependence on the inverse of N_B. This can be equally well seen in the buckling instability of a straight interface [10], wherein the energy of a weakly perturbed interface has the form

$$\mathcal{E}=\mathcal{E}_{\text{straight}}+\int\frac{dk}{2\pi}\Omega(k)|\hat{\zeta}(k)|^2+\cdots\ . \qquad (28)$$

The coefficients $\Omega(k)$ are

$$\Omega(k)=\sigma hk^2-4M^2\{C+\ln(\tfrac{1}{2}hk)+K_0(hk)\}\ , \qquad (29)$$

where K_0 is a Bessel function. If we consider the case of wavelengths long compared to the three-dimensional cutoff, $hk\ll 1$, then we may expand the Bessel function and obtain

$$\Omega\simeq[\sigma h-M^2h^2(1-C)]k^2+M^2h^2k^2\ln(\tfrac{1}{2}hk)\ . \qquad (30)$$

Thus, on purely energetic grounds the most unstable mode is again exponential with the Bond number

$$hk^*\simeq 2e^{C-1/2}e^{-2/N_B}\ . \qquad (31)$$

To the extent that the magnetization is proportional to the applied magnetic field H_0 in an experiment, we have $N_B\propto H_0^2$, providing a simple guide to experiment. Figure 3 shows overlaid plots of the most unstable mode as a function of N_B, obtained from the large-aspect-ratio limit in Eq. (25). Figure 4 displays the same data rescaled by the aspect ratio to yield a dimensionless wave vector $hk^*=2n^*/p$ and plotted semilogarithmically versus $1/N_B$. The good approximation to an exponential is clear, and we see in this limit that there is indeed a well-defined most-unstable wavelength, independent of domain radius. Experiments testing this relation will be reported elsewhere [30].

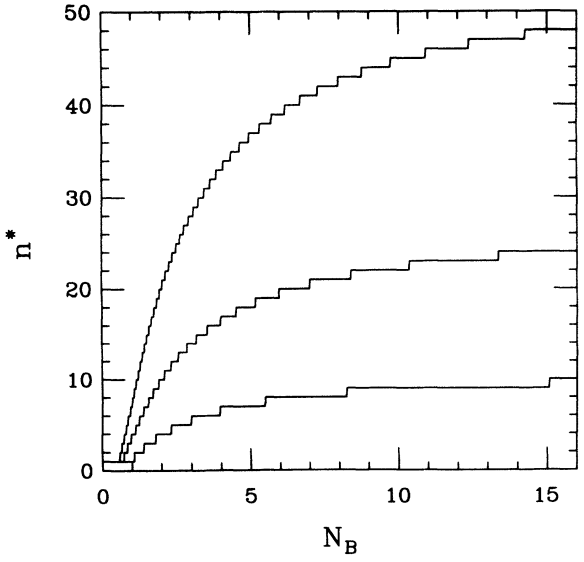

FIG. 3. Fastest-growing mode as a function of Bond number in the limit of large aspect ratios. Shown are results for three different aspect ratios ($p=10$, 25, and 50 from bottom to top).

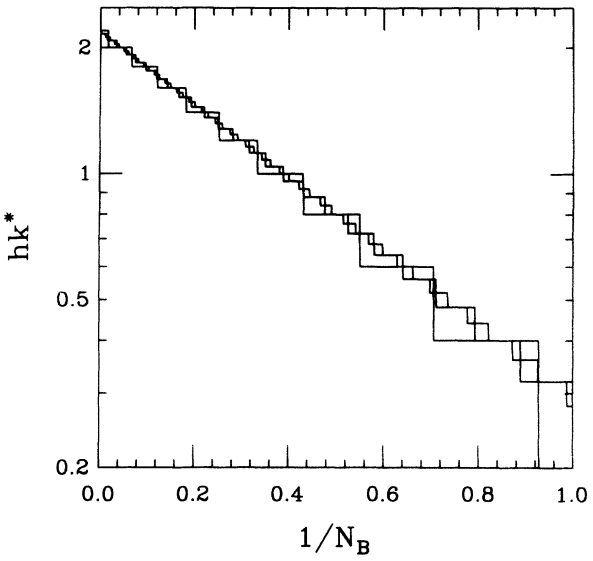

FIG. 4. Dimensionless wave vector k^* with largest growth rate, obtained from graphs in Fig. 3, demonstrating the exponential dependence on the inverse Bond number.

C. Pattern selection

Experiments [12] have revealed that the wavelength of the initial instability of a circular domain depends on the rate at which the magnetic field is ramped through the bifurcation. This is to be expected, since the fastest-growing mode is then itself a function of time. Most striking is the appearance of an approximate scaling law between the initial mode of instability n^* and the ramp rate (dH/dt) of the magnetic field. Thus, if the magnetic field was of the form $H(t)=\beta t$, where β is a constant, then there is a relation of the form

$$n^* \sim \beta^{\psi} , \tag{32}$$

with $\psi \simeq 0.2-0.25$.

To explain this behavior, we first hypothesize that the initial shape is a circle perturbed by a random distribution of modes ζ_n with no n dependence to those amplitudes. Second, we assume that mode selection is complete when some amplitude reaches a critical value. Because the magnetization $M(t)=\chi H(t)$ is time dependent, so too is the growth rate ω_n in the linear stability analysis [31]. This implies that the amplification factor by which the mode n has grown in time t is not simply $\exp(\omega_n t)$, but rather

$$\exp\left[\int_0^t dt' \omega_n(t')\right] . \tag{33}$$

It is then reasonable to expect that the selected mode will be the one that reaches its critical amplitude in the shortest time.

To see the role of the time-dependent magnetic field, consider for the moment an infinite system, replacing modes n by wave vector k, with a simplified growth rate $\omega(k,t)$ having a competition between two terms:

$$\omega(k,t)=a(\beta t)^{\nu} k^m - b k^n , \tag{34}$$

where $n > m$. Integrating with respect to time, and making the additional simplifying assumption that the critical amplitude for mode selection is k independent, we find the time $\tau(k)$ for the mode k to reach criticality is the solution to

$$\frac{a}{\nu+1}\beta^{\nu}\tau(k)^{\nu+1}k^m - \tau(k)k^n = C_1 , \tag{35}$$

with C_1 a constant. Now differentiate with respect to k, and set $d\tau(k)/dk = 0$, and substitute back into (35) to obtain the critical wave vector k^*, which scales with ramp rate as

$$k^* \sim \beta^{\psi}, \quad \psi = \frac{\nu}{n(1+\nu)-m} . \tag{36}$$

In the context of the fully hydrodynamic calculation, the time constant $\tau(n)$ satisfies

$$\frac{h^2}{12\eta R_0^3}|n|\{\sigma(1-n^2)\tau_n + \tfrac{2}{3}h(p\beta\chi)^2\tau_n^3 \mathcal{D}_n(p)\} = C_1 . \tag{37}$$

Figure 5 shows the function τ_n obtained from Eq. (37) for a particular (arbitrary) value of C_1 and three hundredfold multiples of some β_0. The shallow minimum in τ_n clearly moves out with increasing field ramp rate, and, as shown in the inset, displays a good power law with an exponent $\psi \simeq 1/4.2 \simeq 0.24$, in fair agreement with experiments. The fact that $\psi \simeq \frac{1}{4}$ may be understood by recognizing that the experiments probe wave vectors which begin to approach the regime $kh \sim 1$. The fact that the domain is circular is then unimportant, and we may refer to the buckling instability of the edge of a semi-infinite domain described by Eq. (28). In this regime, the magnetic contribution $\mathcal{D}_n$ is dominated by the logarithmic term, so the exponent m in (34) is 1, apart from logarithmic corrections, while the bare surface tension dominates at high k, so $n=3$. From Eq. (37), with $\nu=2$, we find $\psi=\frac{1}{4}$. The data in the inset of Fig. 5, taken from [12] and [32], show the scaling observed for ferrofluid drops of three different initial radii. Although the prefactors of the experimental power laws vary with drop size, the exponent is robust, as is predicted from this analysis.

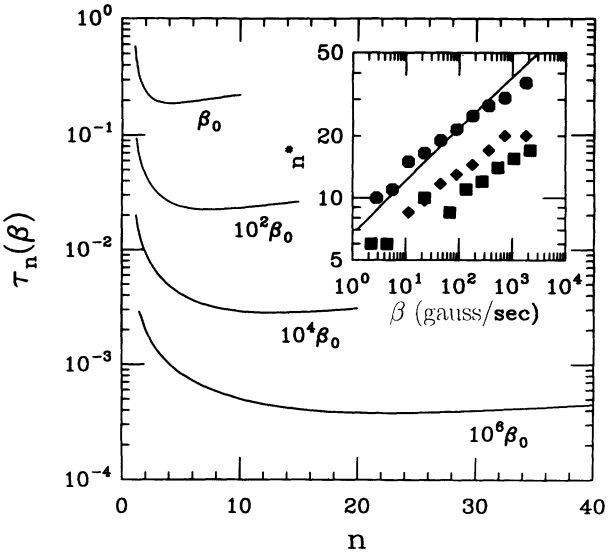

FIG. 5. Curves of τ_n for various ramp rates β. Each curve has a β of 100 times the previous. Note how the mode selection time is reduced for higher ramp rates. The inset shows theoretical results (solid line) and experimental data for $n(\beta)$ [32] on three domains of differing size.

D. Numerical results

Numerical solutions were begun with circular initial states perturbed by a small amount of random noise distributed in the first eight azimuthal modes. The evolution was then accomplished by Euler stepping forward in time, respacing the points after each iteration. We also increased the number of points periodically in order to preserve accuracy, but kept as few as possible in the interest of speed. A typical simulation begins with a grid of 64 points and ends with 512, taking on the order of 250 mflop h. Computationally, it was inconvenient to use ramp rates leading to final states of high complexity, so most of our results are for relatively simple shapes and are summarized in Fig. 1. There is certainly a qualitative resemblance between the experimental and theoretical shapes, and, indeed, faster ramp rates do indeed result in higher complexity. We are also encouraged by the constant arm width, which depends on the final field value, and the slightly bulbous ends.

Figures 6 and 7 show overlaid contours from the near-circular initial shape to a branched figure in the late stages of the dynamics. As in experiment, we see quite rapid evolution from the circle to a particular branched geometry, followed by a more gradual spreading of the pattern primarily accomplished by motion at the tips of the fingers and accompanied by a gradual thinning of

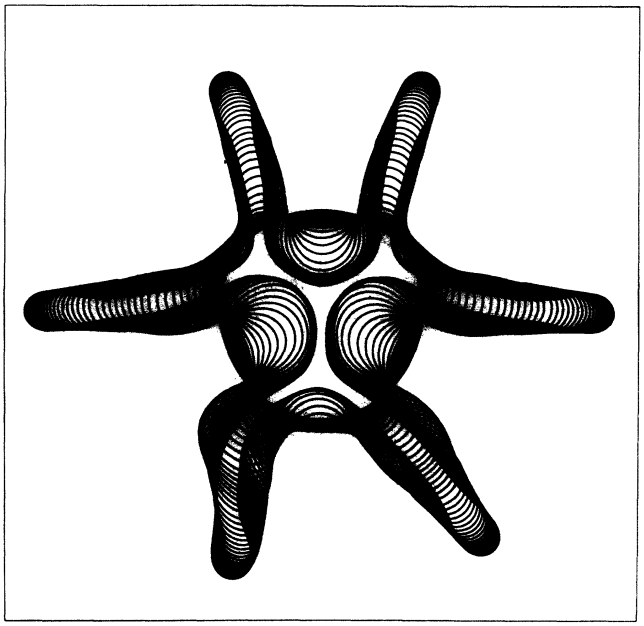

FIG. 6. Fingering instability from conformal mapping solution, overlaid in time to illustrate the stages of shape evolution. The initial near-circular shape has aspect ratio $p=2.0$, and the evolution takes place for $N_B=21$.

their widths.

Finally, while it was quite clear that the experimentally obtained final states were stable, it was a much more difficult task to determine this computationally. We ended up stopping the routine when the motion had slowed down considerably from its peak value (at least an order of magnitude). In some sense, this is equivalent to the addition of an extra "sticking force" of some kind, which probably exists to some degree experimentally; however, it does make it impossible to say for sure whether the theoretical final states are truly stationary, or just *extremely* slowly varying.

IV. CONCLUSIONS

While the present work has addressed the shape instabilities and dynamics of a *single* magnetic domain, we suggest that these results have bearing on the complex many-domain problem often encountered in magnetic and superconducting systems. The range of morphologies observed, from well-ordered stripe patterns to intricately interdigitated branched structures, mirrors those seen in single domains. We suggest that a fruitful approach to the many-domain problem, from both conceptual and calculational points of view, is its reduction to a many-interface representation. Indeed, the competition between surface tension and Biot-Savart forces studied here emerges as a particular limit of the interface motion appropriate to the Ginzburg-Landau model for superconductors [33].

The simplest energetic model [34] for the many-domain problem would be the generalization of Eq. (10) to a set of *interacting current loops* whose positions are given by the set of vectors $\{\mathbf{r}_i\}$,

$$\mathcal{E}[\{\mathbf{r}_i\}]=\sum_i \gamma L_i - \tfrac{1}{2}\sum_{i,j} M^2 h \oint ds_i \oint ds_j' \hat{\mathbf{t}}(s_i)\cdot\hat{\mathbf{t}}(s_j') \times \Phi(|\mathbf{r}(s_i)-\mathbf{r}(s_j')|/h)\ , \tag{38}$$

where L_i is the length of a given loop and the second sum runs over all pairs of loops, each loop traversed in the same direction. In its application to type-I superconductors, additional terms proportional to the area of each loop would be present, reflecting the difference in free energy between the bulk superconducting and normal states.

This simplified representation should allow one to understand how the interactions between domains affects the shape transitions of each, particularly as they relate to the collective instabilities of ordered arrays such as stripes and bubbles. While it appears that detailed numerical study of a model with such long-range interactions will require significant computational effort, recent work on spectral approaches to the associated vortex sheet calculations [35], coupled with fast-summation techniques and multipole expansions for far-field contributions, should make this study tractable.

Finally, it is of interest to address the hydrodynamics of fingering instabilities in amphiphilic monolayers. Here, one may consider a very simple model based on Stokes flow in two dimensions, where the balance between viscous dissipation and pressure takes the form

$$\mu\nabla^2\mathbf{v}=\nabla P\ . \tag{39}$$

The linear stability problem in this limit has recently been considered, while the full interface problem is under active study [36], as is the coupling between the in-plane

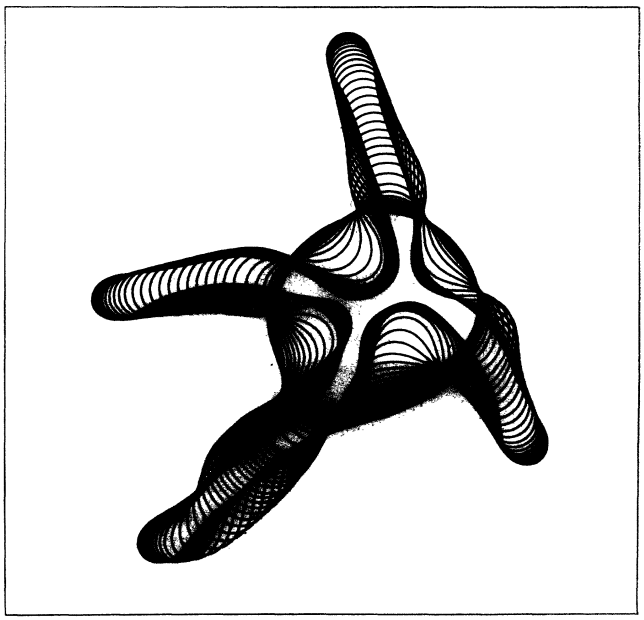

FIG. 7. As in Fig. 6, but for a different initial condition.

flow and that of the underlying fluid [37]. Inclusion of thermal fluctuations into such hydrodynamic approaches should allow for the study of finite-temperature fluctuating interface dynamics. A simpler dynamical approach described elsewhere [38] begins to address the effects of thermal fluctuations in dipolar systems.

ACKNOWLEDGMENTS

We thank A. J. Dickstein, S. Erramilli, and S. A. Langer for ongoing collaborations, and A. T. Dorsey, T. C. Halsey, H. M. McConnell, N. P. Ong, D. M. Petrich, R. E. Rosensweig, M. Seul, and M. J. Shelley for important discussions. H. M. McConnell and J. Warren have kindly communicated results prior to publication. This work was supported in part by the NSF PFF Grant No. DMR-9350227 and the Alfred P. Sloan Foundation (R.E.G.).

APPENDIX A: BOUNDARY INTEGRAL METHOD FOR GENERALIZED DARCY'S LAW

Here we provide a brief discussion of the vortex sheet representation for Hele-Shaw flow, generalizing existing analyses for motion driven by surface tension and an external gravitational force [39]. First, observe from Darcy's law that the tangential components of the fluid velocity are related to the pressure boundary condition through

$$\hat{\mathbf{t}}\cdot(\nabla\Pi_2-\nabla\Pi_1)|_{\mathcal{C}}=-\hat{\mathbf{t}}\cdot\left[\frac{12\eta_2}{h^2}\mathbf{v}_2-\frac{12\eta_1}{h^2}\mathbf{v}_1\right] . \quad \text{(A1)}$$

Define the average fluid velocity $\mathbf{V}=(\mathbf{v}_1+\mathbf{v}_2)/2$, average viscosity $\bar{\eta}=(\eta_1+\eta_2)/2$, and viscosity Atwood ratio

$$A_\eta=\frac{\eta_1-\eta_2}{\eta_1+\eta_2} . \quad \text{(A2)}$$

Then (A1) becomes

$$\partial_s(\Delta\Pi)=-\frac{12\bar{\eta}}{h^2}[\hat{\mathbf{t}}\cdot(\mathbf{v}_1-\mathbf{v}_2)-2A_\eta\hat{\mathbf{t}}\cdot\mathbf{V}] . \quad \text{(A3)}$$

The pressure jump $\Delta\Pi$ is given by Eq. (5), while the tangential velocity discontinuity gives the vortex sheet strength $\gamma=\hat{\mathbf{t}}\cdot(\mathbf{v}_2-\mathbf{v}_1)$. In addition, the mean velocity $\mathbf{V}$ is given by the Birkhoff-Rott integral [40]

$$\mathbf{V}(s)=\frac{1}{2\pi}\mathrm{P}\int ds'\frac{\hat{\mathbf{e}}_z\times[\mathbf{r}(s)-\mathbf{r}(s')]}{|\mathbf{r}(s)-\mathbf{r}(s')|^2}\gamma(s')ds' , \quad \text{(A4)}$$

where P means a principal-value integral. Hence, the vortex sheet strength solves the integral equation

$$\gamma(s)-2A_\eta\frac{1}{2\pi}\mathrm{P}\int ds'\frac{\hat{\mathbf{e}}_z\times[\mathbf{r}(s)-\mathbf{r}(s')]}{|\mathbf{r}(s)-\mathbf{r}(s')|^2}\gamma(s')ds' = -\frac{h^2}{12\eta}\left[\sigma\kappa_s+\frac{2M^2}{h}I_s\right] . \quad \text{(A5)}$$

In the simplest case of zero viscosity contrast ($A_\eta=0$), we see that the integral equation simplifies to give the vortex sheet strength directly in terms of the competing Young-Laplace and Biot-Savart forces.

APPENDIX B: EQUIVALENCE OF TWO EXPRESSIONS FOR THE MAGNETIC PRESSURE

In this appendix we show the equivalence between the two expressions for the magnetic integral $I(s)$, Eqs. (6) and (7),

$$I(s)=\oint_{\mathcal{C}} ds'\hat{\mathbf{R}}\times\hat{\mathbf{t}}(s')[-1+\sqrt{1+(h/R)^2}] \equiv I_1+I_2 \quad \text{(B1)}$$

and

$$I'(s)=\int_{\mathcal{D}} dA'\left[\frac{1}{R}-\frac{1}{\sqrt{R^2+h^2}}\right] , \equiv I'_1+I'_2 , \quad \text{(B2)}$$

which follow, respectively, from the alternative views of magnetization as arising from magnetic "charge" and circulating currents. Here,

$$R=\sqrt{(x-x')^2+(y-y')^2} ,$$

and in (B1) points on the contour ar given by the vectors $\mathbf{r}(s)=(x,y)$ and $\mathbf{r}(s')=(x',y')$, with $x=x(s)$, $x'=x(s')$, etc. In (B2) the primed coordinates x' and y' are integration variables *within* the domain.

To begin, note that $\hat{\mathbf{t}}(s')=(x_{s'},y_{s'})$, and thus

$$I_1(s)=-\oint_{\mathcal{C}} ds'\frac{(x-x')y'_{s'}-(y-y')x'_{s'}}{\sqrt{(x-x')^2+(y-y')^2}} . \quad \text{(B3)}$$

The equivalence with I'_1 is shown first by using the Stokes theorem

$$\oint_{\mathcal{C}}\mathbf{F}\cdot d\mathbf{l}'=\int_{\mathcal{D}} dA'(\nabla\times\mathbf{F})\cdot\hat{\mathbf{n}} ,$$

with $\nabla\times\mathbf{F}=R^{-1}\hat{\mathbf{e}}_z$. The vector $\mathbf{F}$ may be written as $\mathbf{F}=f(x,y|x',y')\hat{\mathbf{e}}_x$, with

$$f(x,y|x',y')=\ln[y-y'+R] , \quad \text{(B4)}$$

or as

$$\mathbf{F}=-f(y,x|y',x')\hat{\mathbf{e}}_y ,$$

or, more symmetrically, as one-half the sum of these. We then obtain

$$I'_1(s)=\oint_{\mathcal{C}} ds'x'_{s'}\ln[(y-y')+R] . \quad \text{(B5)}$$

An integration by parts yields

$$I'_1=\oint ds'(x-x')\frac{d}{ds'}\{\ln[(y-y')+R]\} . \quad \text{(B6)}$$

After carrying through the differentiation, performing a number of rearrangements easily recovers Eq. (B3), demonstrating that $I_1=I'_1$.

To relate the integrals I_2 and I'_2, we first write

$$I_2(s)=\oint_{\mathcal{C}} ds'\frac{\mathbf{R}\times\hat{\mathbf{t}}(s')}{R^2}\sqrt{R^2+h^2} , \quad \text{(B7)}$$

and note that $\mathbf{R}\times\hat{\mathbf{t}}(s')=\mathbf{R}\cdot\hat{\mathbf{n}}(s')$. Further, since $\nabla'[\ln(R)]=-\mathbf{R}/R^2$,

$$I_2=-\oint_{\mathcal{C}} ds'\hat{\mathbf{n}}'\cdot\nabla'(\ln R)\sqrt{R^2+h^2}\ , \tag{B8}$$

By Green's identity, we then have

$$I_2=-\int_{\mathcal{D}} dA'[\sqrt{R^2+h^2}\nabla'^2(\ln R) + \nabla'(\ln R)\cdot\nabla'\sqrt{R^2+h^2}]\ . \tag{B9}$$

Since $\nabla'^2(\ln R)=0$, we obtain $I_2=I_2'$.

Finally, we discuss the relationship between the magnetic integrals entering the energy and boundary conditions and those familiar from treatments of the self-induction and Biot-Savart force on current-carrying wires [21,41]. We recall first that the magnetic energy in Eq. (10) arises from integrations over the thickness of the slab of a Coulombic interaction between the tangent vectors to the boundary [14,24],

$$\mathcal{E}=-M^2\int_0^h dz\oint_{\mathcal{C}} ds\int_0^h dz'\oint_{\mathcal{C}} ds'\frac{\hat{\mathbf{t}}(s)\cdot\hat{\mathbf{t}}(s')}{|\mathbf{r}(s,z)-r(s',z')|}\ , \tag{B10}$$

This is fully equivalent to the general formula for the magnetostatic energy due to currents $\mathbf{j}(\mathbf{r})$ [41]:

$$\mathcal{E}=-\frac{1}{2c^2}\int d^3r\int d^3r'\frac{\mathbf{j}(\mathbf{r})\cdot\mathbf{j}(\mathbf{r}')}{|\mathbf{r}-\mathbf{r}'|}\ , \tag{B11}$$

if we take the currents to have magnitude $|\mathbf{j}|=cM$ per unit height and be confined to the ribbon-shaped boundary of the slab. For distances $|\mathbf{r}(s)-\mathbf{r}(s')|$ large compared to h, the self-induction integral is approximately

$$\mathcal{E}\simeq-\tfrac{1}{2}M^2h^2\oint_{\mathcal{C}} ds\oint_{\mathcal{C}} ds'\frac{\hat{\mathbf{t}}(s)\cdot\hat{\mathbf{t}}(s')}{|\mathbf{r}(s)-\mathbf{r}(s')|}\ , \tag{B12}$$

the familiar form for wires of negligible thickness.

The force integral, Eq. (7), also simplifies in this limit, giving a pressure

$$U(s)=-M^2h^2\oint ds'\frac{[\mathbf{r}(s)-\mathbf{r}(s')]}{|\mathbf{r}(s)-\mathbf{r}(s')|^3}\times\hat{\mathbf{t}}(s')\ , \tag{B13}$$

the familiar Biot-Savart force which is partner to (B12).

[1] *Hydrodynamic Instabilities and the Transition to Turbulence,* 2nd ed., edited by H. L. Swinney and J. P. Gollub (Springer-Verlag, New York, 1985).

[2] P. G. Saffman and G. I. Taylor, Proc. R. Soc. London, Ser. A **245**, 312 (1958).

[3] T. A. Witten, Jr. and L. M. Sander, Phys. Rev. Lett. **47**, 1400 (1981).

[4] F. Melo, J. F. Joanny, and S. Fauve, Phys. Rev. Lett. **63**, 1958 (1989).

[5] P. Constantin, T. F. Dupont, R. E. Goldstein, L. P. Kadanoff, M. J. Shelley, and S. M. Zhou, Phys. Rev. E **47**, 4169 (1993).

[6] R. E. Rosensweig, *Ferrohydrodynamics* (Cambridge University Press, Cambridge, England, 1985), and references therein.

[7] R. E. Rosensweig, M. Zahn, and R. Shumovich, J. Magn. Magn. Mater. **39**, 127 (1983).

[8] H. Möhwald, Annu. Rev. Phys. Chem. **41**, 441 (1990).

[9] H. M. McConnell, Annu. Rev. Phys. Chem. **42**, 171 (1991).

[10] A. O. Tsebers and M. M. Maiorov, Magnetohydrodynamics **16**, 21 (1980).

[11] A. G. Boudouvis, J. L. Puchalla, and L. E. Scriven, J. Colloid Interface Sci. **124**, 688 (1988).

[12] A. J. Dickenstein, S. Erramilli, R. E. Goldstein, D. P. Jackson, and S. A. Langer, Science **261**, 1012 (1993).

[13] K. Y. C. Lee and H. M. McConnell, J. Phys. Chem. **97**, 9532 (1993).

[14] S. A. Langer, R. E. Goldstein, and D. P. Jackson, Phys. Rev. A **46**, 4894 (1992).

[15] G. K. Batchelor, *An Introduction to Fluid Dynamics* (Cambridge University Press, Cambridge, England, 1967), pp. 222–224.

[16] D. Bensimon, L. P. Kadanoff, S. Liang, B. I. Shraiman, and C. Tang, Rev. Mod. Phys. **58**, 977 (1986).

[17] R. C. Sherwood, J. P. Remeika, and H. J. Williams, J. Appl. Phys. **30**, 217 (1959).

[18] R. P. Huebener, *Magnetic Flux Structures in Superconductors* (Springer-Verlag, New York, 1979).

[19] D. J. Keller, J. P. Korb, and H. M. McConnell, J. Phys. Chem. **91**, 6417 (1987).

[20] J. M. Deutch and F. E. Low, J. Phys. Chem. **96**, 7097 (1992).

[21] See, for example, J. D. Jackson, *Classical Electrodynamics,* 2nd ed. (Wiley, New York, 1975).

[22] A. O. Tsebers and A. A. Zemitis, Magnetohydrodynamics **19**, 360 (1983).

[23] D. A. Kessler and H. Levine, Phys. Rev. Lett. **67**, 3121 (1991).

[24] A. O. Tsebers, Magnetohydrodynamics **25**, 149 (1989).

[25] We are grateful to M. J. Shelley for discussions concerning this point.

[26] R. E. Goldstein, A. I. Pesci, and M. J. Shelley, Phys. Rev. Lett. **70**, 3043 (1993).

[27] See also Ref. [13].

[28] A. A. Thiele, Bell Syst. Tech. J. **48**, 3287 (1969).

[29] R. de Koker and H. M. McConnell, J. Phys. Chem. (to be published).

[30] Timothy Gardner, Shyamsunder Erramilli, and Raymond E. Goldstein (unpublished).

[31] This approach is similar in spirit to a recent analysis of wavelength selection in directional solidification in which the importance of the initial transients was emphasized. See J. A. Warren and J. S. Langer, Phys. Rev. E **47**, 2702 (1993).

[32] A. J. Dickstein, S. Erramilli, and R. E. Goldstein (unpublished).

[33] A. T. Dorsey, Ann. Phys. N. Y. (to be published).

[34] R. E. Goldstein, D. P. Jackson, and A. T. Dorsey (unpublished).

[35] J. Lowengrub (private communication).

[36] D. Lubensky and R. E. Goldstein (unpublished).

[37] H. A. Stone and H. M. McConnell (unpublished).
[38] R. E. Goldstein and D. P. Jackson (unpublished).
[39] See, e.g., G. Tryggvason and H. Aref, J. Fluid Mech. **136**, 1 (1983); W. Dai and M. J. Shelley, Phys. Fluids A **5**, 2131 (1993).
[40] G. Birkhoff, Los Alamos Scientific Laboratory Report No. LA-1862, 1954 (unpublished).
[41] L. D. Landau and E. M. Lifshitz, *Electrodynamics of Continuous Media,* 2nd ed. (Pergamon, New York, 1984), pp. 119.

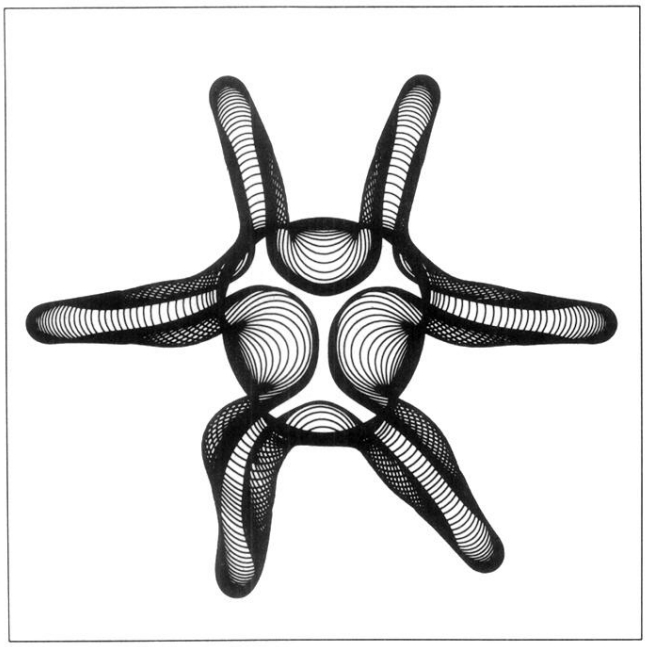

FIG. 6. Fingering instability from conformal mapping solution, overlaid in time to illustrate the stages of shape evolution. The initial near-circular shape has aspect ratio $p=2.0$, and the evolution takes place for $N_B=21$.

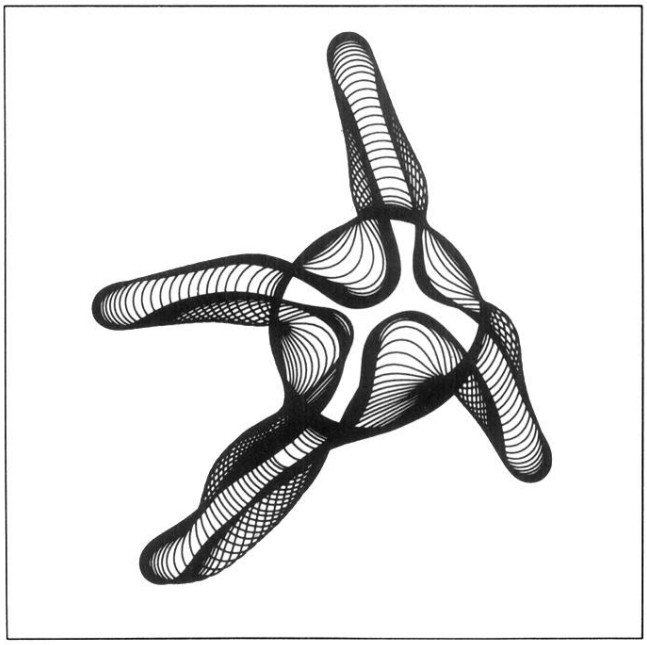

FIG. 7. As in Fig. 6, but for a different initial condition.